

1        **When there is no offset – a demonstration of seismic**  
2        **diffraction imaging and depth-velocity model building**  
3        **in the southern Aegean Sea**

4        **J. Preine<sup>1</sup>, B. Schwarz<sup>2</sup>, A. Bauer<sup>1</sup>, and C. Hübcher<sup>1</sup>**

5                    <sup>1</sup>Institute of Geophysics, University of Hamburg, Hamburg, Germany  
6                    <sup>2</sup>GFZ German Research Centre for Geosciences, Potsdam, Germany

7        **Key Points:**

- 8        • Based on waveform similarities we surgically extract a detail-rich diffracted wave-  
9        field from zero-offset seismic data from the Aegean Sea  
10       • Fully driven by data, we infer a laterally resolved velocity model from zero-offset  
11       information through diffraction wavefront tomography  
12       • After interpretation-guided refinement, we derive depth-migrated reflection and  
13       diffraction images which we use for interpretation

---

Corresponding author: Jonas Preine, [jonas.preine@uni-hamburg.de](mailto:jonas.preine@uni-hamburg.de)

**Abstract**

A vast majority of marine geological research is based on academic seismic data collected with single-channel systems or short-offset multi-channel seismic cables, which often lack reflection moveout for conventional velocity analysis. Consequently, our understanding of earth processes often relies on seismic time sections, which hampers quantitative analysis in terms of depth, formation thicknesses, or dip angles of faults. In order to overcome these limitations, we present a robust diffraction extraction scheme that models and adaptively subtracts the reflected wavefield from the data. We use diffractions to estimate insightful wavefront attributes and perform wavefront tomography to obtain laterally resolved seismic velocity information in depth. Using diffraction focusing as a quality control tool, we perform an interpretation-driven refinement to derive a geologically plausible depth-velocity-model. In a final step, we perform depth migration to arrive at a spatial reconstruction of the shallow crust. Further, we focus the diffracted wavefield to demonstrate how these diffraction images can be used as physics-guided attribute maps to support the identification of faults and unconformities. We demonstrate the potential of this processing scheme by its application to a seismic line from the Santorini-Amorgos Tectonic Zone, located on the Hellenic Volcanic Arc, which is notorious for its catastrophic volcanic eruptions, earthquakes, and tsunamis. The resulting depth image allows a refined fault pattern delineation and, for the first time, a quantitative analysis of the basin stratigraphy. We conclude that diffraction-based data analysis is a decisive factor, especially when the acquisition geometry of seismic data does not allow conventional velocity analysis.

**Plain Language Summary**

The active seismic method is a standard tool for studying and imaging the Earth's lithosphere. Proper imaging of complex geological targets requires seismic data of excellent quality, which are typically only acquired with expensive industrial surveys. Academic surveys, however, are often restricted to marine seismic equipment with limited illumination, which compromises imaging and interpretation. While most of the contemporary processing and interpretational routines are tailored to the reflected wavefield, recent research suggests that the often overlooked diffracted wavefield might help to overcome the gap between academic and industrial seismic imaging. Wave diffraction is the response of the seismic wavefield to small-scale subsurface structures and allows to estimate velocities even from single-channel seismic data.

In this study, we use an academic seismic profile from the southern Aegean Sea and extract a rich diffracted wavefield from the data. We utilize these diffractions to estimate a velocity model that permits a reconstruction of the subsurface in depth and specifically highlight discontinuous features related to past dynamic processes. Such depth images allow us to reliably measure thicknesses and fault angles. We conclude that diffraction-based data analysis is a decisive factor for academic research and strongly encourage its application in future studies.

## 1 Introduction

Most marine geological research during the last 50 years is based on academic seismic reflection data, collected with single-channel systems or multi-channel seismic cables with an offset-depth ratio too small for velocity analysis based on common-midpoint (CMP) processing. Without doubt, the scientific outcome from those studies is impressive, yet, seismic depth sections would be required in order to test them by quantitative modeling. In recent works, it has been shown that diffractions possess unique properties which bear the potential to overcome these characteristic limitations of academic studies (e.g. Bauer et al., 2017; Schwarz & Gajewski, 2017; Fomel et al., 2007). Wave diffraction occurs at geodynamically important structures like faults, pinch-outs, erosional surfaces, or other small-scale scattering objects and encodes sub-wavelength information on the scattering geometry (e.g. Landa & Keydar, 1998). Diffracted waves do not obey Snell's Law and provide superior illumination compared to reflected waves. Moreover, due to their passive-source like radiation, they encode their full multi-channel response in prominent data subsets like the zero-offset section (e.g. Bauer et al., 2017; Schwarz & Gajewski, 2017).

Separating the diffracted wavefield has high potential: on the one hand, it principally allows to image and analyze fault systems as well as the small-scale heterogeneity of the rift basins with sub-wavelength resolution (Berkovitch et al., 2009; Silvestrov et al., 2015; Decker et al., 2015). On the other hand, diffractions illuminate the subsurface in such a way that laterally resolved velocity information can be obtained. Consequently, and without the need for expensive industry-style acquisitions, diffractions offer the possibility to measure curvatures in the zero-offset section, which allows automatic depth-velocity model building by means of wavefront tomography (Bauer et al., 2017; Duvencq, 2004). However, apart from Bauer et al. (2018) and Bauer et al. (2020), no example of data-driven depth velocity-model building based on diffraction-only data in the zero-offset domain has been published so far.

In this work, we use an academic seismic profile from the Santorini-Amorgos Tectonic Zone (SATZ), located in the South Aegean Sea, to explore the diffracted wavefield and to estimate an interval velocity model for depth-conversion. The SATZ is a typical example for the aforementioned dilemma academic science is often facing. While this area is notorious for its catastrophic volcanic eruptions, earthquakes, and tsunamis, the acting tectonic forces are not completely understood to this day. One reason is that previous studies have been based on single-channel or low-fold seismic vintage data with short streamers (Perissoratis 1995; Hübscher et al., 2006; Nomikou et al., 2018), thus handicapping the estimation of interval-velocities for depth migration. Hübscher et al. (2015) and Nomikou et al. (2018) have shown that the SATZ is characterized by a high degree of local heterogeneity, e.g. in the form of abundant fault systems and volcanic intercalations which makes this area a natural laboratory for studying diffractions.

## 2 Geological setting

The Santorini-Amorgos Tectonic Zone (SATZ) represents a zone of NE-SW oriented en-echelon rifts located in the center of the Hellenic Volcanic Arc in the south Aegean Sea (Figure 1a) (Nomikou et al., 2019). Driven by the rollback of the Nubian slab, the southern Aegean Sea has experienced substantial extension (e.g. Le Pichon & Angelier, 1979; Cossette et al., 2016; Bocchini et al., 2018). The SATZ represents one of the most prominent morphotectonic features of the Cycladic Islands and separates the Cycladic plateau towards the North and the minor Anafi-Astypalaea plateau towards the South (Nomikou et al., 2019; Le Pichon & Kremer, 2010). Bathymetric and available tectonic data of the SATZ most recently published by Nomikou et al. (2019) and Hooft et al. (2017) reveal a system of ridges and basins which has been interpreted as an extensional complex of tectonic grabens and horsts. To the south-west, the SATZ is characterized by the volcanic centers of Christiana, Santorini, and Kolumbo which are responsible for numer-

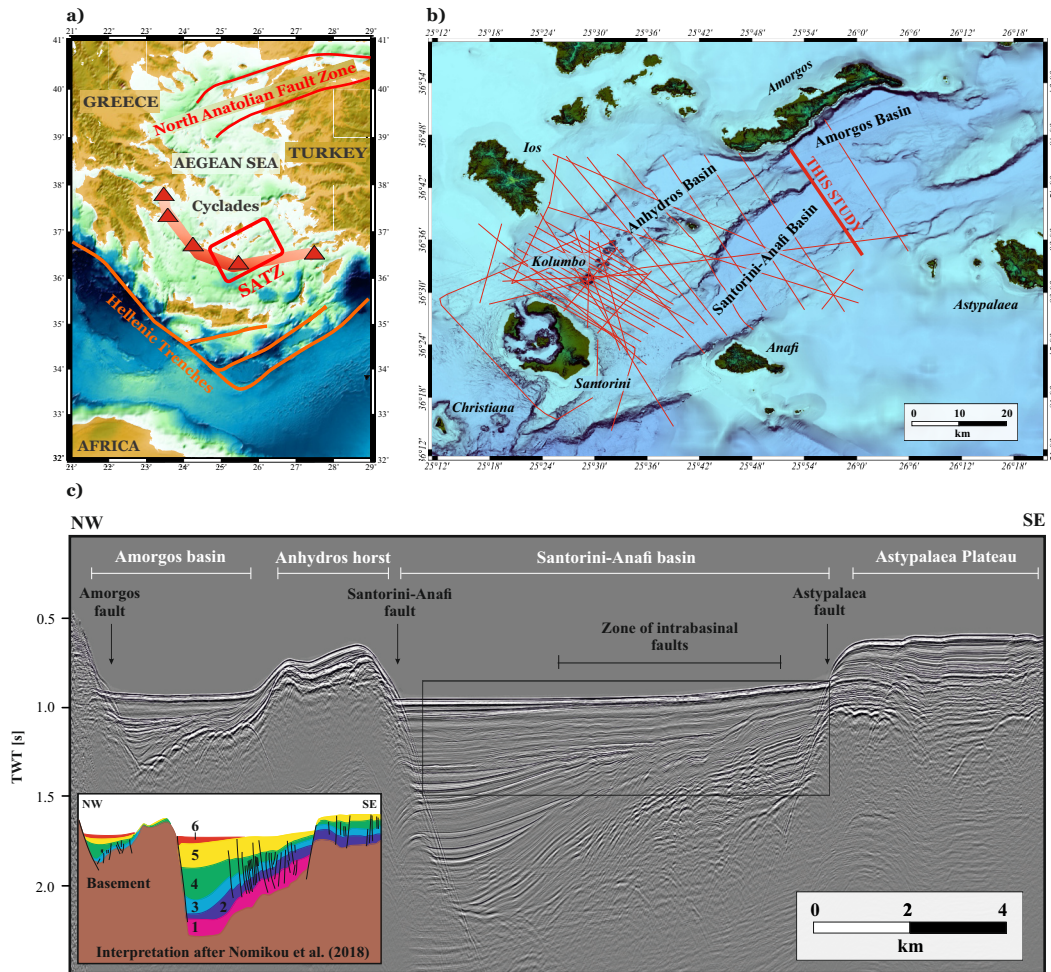


**Figure 1.** (a) Aegean Sea and major geological features. The semi-transparent red area marks the Hellenic Volcanic Arc and the red box indicates the working area. (b) Morphological map of the study area based on swath bathymetry. Thin red lines illustrate the location of the seismic profiles acquired during research cruise POS338 (Hübscher et al., 2006). The thick red line indicates profile 11 which is the focus of this study. (c) CMP Stack of seismic profile 11 after multiple elimination with the interpretation by Nomikou et al. (2018). The black rectangle indicates the location of the blow-up highlighted in Figure 3.

106       ous volcanic eruptions, including the well-known Minoan eruption of Santorini approx.  
 107       3600 years ago (Druitt & Francaviglia, 1992; Druitt et al., 1999; Nomikou, Druitt, et al.,  
 108       2016; Hooft et al., 2019). The remarkably linear alignment of the volcanic edifices high-  
 109       lights the fundamental control that crustal structure and tectonics have on the location  
 110       of volcanic activity (Nomikou et al., 2013, 2019; Hooft et al., 2019; Heath et al., 2019).

111       North-east of Santorini, three distinct basins have been identified by Nomikou et  
 112       al. (2018): the Anhydros basin, the Santorini-Anafi basin, and the Amorgos basin (Fig-  
 113       ure 1b). Seismic reflection data show that the opening of these basins most likely occurred  
 114       in sudden tectonic pulses (Hübscher et al., 2015; Nomikou, Hübscher, et al., 2016). The  
 115       regional geological setting comprises alpine formations forming the basement rocks and  
 116       overlying post-alpine sediments which are restricted to offshore areas between the islands  
 117       and are thought to consist of marine sediments comprising turbidites, hemipelagic sed-  
 118       iments, and volcanoclastics (Perissoratis, 1995; Hübscher et al., 2015; Nomikou, Hübscher,

et al., 2016; Nomikou et al., 2018). These sediments have transgressed the former Cycladic land and volcanic intercalations have been identified close to the volcanic centers of Santorini and Kolumbo (Hübscher et al., 2015; Nomikou, Hübscher, et al., 2016). Each basin is bounded by active marginal normal faults and characterized by extensive internal fault systems (Hübscher et al., 2015; Nomikou et al., 2018).

Based on a recent active seismic tomography experiment, Heath et al. (2019) and Hooft et al. (2019) obtained tomographic P-wave velocity models for the upper-crustal structure across Santorini volcano and the surrounding region. In agreement with the previous tectonic models, they conclude that tectono-magmatic lineaments control magma emplacement at Santorini and Kolumbo and that the initiation of basin-formation predates the onset of volcanism. Heath et al. (2019) inferred that the Anhydros Basin is of maximum 1.5 km thickness and the Santorini-Anafi Basin of maximum 2 km thickness.

There is an ongoing debate about the role of strike-slip deformation in the SATZ. Based on the investigation of microseismic activity, Bohnhoff et al. (2006) concluded that the SATZ is currently influenced by a right-lateral transtensional tectonic regime. Sakellariou et al. (2010) proposed the concept that the whole SATZ represents a shear zone characterized by dextral strike-slip to oblique faults. Direct seismic indicators like flower structures, however, have not been presented so far. Also recent publications by Hübscher et al. (2015) and Nomikou et al. (2018) did not find direct indicators for strike-slip faulting in the presented multi-channel reflection seismic data. While the possibility of strike-slip faulting was not ruled out, these authors concluded that normal faulting as a result of the regional extensional to transtensional movement represents the main tectonic mechanism.

### 3 Imaging challenges

In order to further investigate the role of strike-slip tectonics and to understand the dynamics of the basin formation, seismic imaging in depth is necessary to properly estimate sedimentary thicknesses, calculate fault angles, and quantify horizontal strain. To arrive at accurate reconstructions in depth, precise velocity models, which require borehole information and lateral illumination, are in demand. Typically, this is achieved by means of deploying long streamers as they are used e.g. in hydrocarbon industry. Academic surveys, however, are often very limited in terms of budget and, therefore, mostly smaller streamer systems with lower channel-counts are used aggravating the estimation of interval velocities.

This dilemma also applies to the SATZ. On the one hand, there are no exploitable boreholes in the area that could serve as a reliable source for velocity information. On the other hand, available academic reflection seismic data from the SATZ is generally of poor quality. Pioneering work by Perissoratis (1995) was based on analog data acquired with a single-channel streamer and even recent studies by Sakellariou et al. (2010) and Tsampouraki-Kraounaki and Sakellariou (2018) were based on digital single-channel seismic data. In contrast, the stratigraphic studies by Hübscher et al. (2015) and Nomikou, Hübscher, et al. (2016); Nomikou et al. (2018, 2019) were based on multi-channel seismic data collected in 2006 during research cruise POS338 with RV Poseidon using a streamer of 600 m length (Hübscher et al., 2006). While the resulting data-quality was superior compared to previous studies, the relatively large channel spacing of 25 m limited a detailed investigation of internal reflection and fault patterns and the limited streamer length hampered the estimation of velocities from the data. Another source of uncertainty of these data regarding the estimation of interval velocities is the fact that no birds were used during the measurement to control the depth of the streamer.

Therefore, the only available velocity information from the SATZ are the tomographic P-wave velocity models presented by Heath et al. (2019) and Hooft et al. (2019). While these models are well suited to study the large-scale structure of the upper <3 km crust, they do not resolve the small-scale velocity distribution and do not account for the high

171 degree of local complexity in the rift basins. Consequently, these velocity models can-  
 172 not be used directly for depth migration.

173 Figure 1c shows a CMP stack of seismic line 11 from POS338 data-set after the ap-  
 174 plication of surface-related multiple elimination (SRME) (Verschuur et al., 1992). This  
 175 profile has been interpreted by Nomikou et al. (2018) and runs NW-SE crossing the Amor-  
 176 gos basin, the Anhydros Horst as well as the Santorini-Anafi basin and the Astypalaea  
 177 plateau. The Amorgos basin is interpreted as a semi-graben produced by the activity  
 178 of the Amorgos fault, whereas the Santorini-Anafi basin represents an asymmetric graben  
 179 bounded by the important Santorini-Anafi fault and the Astypalaea fault (Nomikou et  
 180 al., 2018). Six sedimentary units were identified within the Santorini-Anafi basin and ma-  
 181 jor internal deformation is indicated by extended fault systems in the sedimentary strata  
 182 of the Santorini-Anafi basin within the hinge-zone of the marginal Santorini-Anafi fault  
 183 and the Astypalaea fault (see small illustration in Figure 1c). These fault systems are  
 184 associated with a high number of diffractions which are overprinted by the dominant re-  
 185 flected wavefield. The abundance of diffractions makes this seismic profile a highly suit-  
 186 able example to test how the diffracted wavefield can contribute to the processing and  
 187 interpretation of offset-limited academic seismic data.

## 188 4 Methods

189 In recent decades, detail-rich seismic wavefields have been captured on land and  
 190 on the sea. Owing to its first development and extensive utilization in the prospection  
 191 of oil and gas, until the early 2000s, the seismic method put most emphasis on the re-  
 192 flected portion of this wavefield, which resulted in many important discoveries in indus-  
 193 try and academia. With the advent of full-waveform inversion, the desire to record low-  
 194 frequency diving waves led to a spectacular yet cost-intensive shift in data acquisition  
 195 (Virieux & Operto, 2009; Warner et al., 2013; Morgan et al., 2013). As a result, the promised  
 196 resolution of such reconstructions remains largely intractable in expeditions where aca-  
 197 demic objectives are concerned. To arrive at maximally resolved seismic subsurface re-  
 198 constructions when academic low-fold and short-offset acquisitions were recorded, we make  
 199 use of the still largely unexplored diffracted component of the wavefield (e.g. Schwarz,  
 200 2019b). As illustrated in Figure 2a, diffractions are unique in that they exclusively oc-  
 201 cur when subsurface properties change abruptly. More precisely, in contrast to reflec-  
 202 tions and diving waves, these signatures are only caused, when the local curvature of a  
 203 material contrast is comparable to or even smaller than the prevailing seismic wavelength.  
 204

### 205 4.1 Diffraction separation and focusing

206 Owing to the effect of geometrical spreading, diffractions are generally character-  
 207 ized by very low amplitudes and often remain masked by more prominent higher-amplitude  
 208 reflections (Figure 2a). For that reason, accessing the diffracted wavefield has been and  
 209 still remains a major challenge to confront. In recent years, a range of methods has been  
 210 introduced to arrive at approximate diffraction-only images based e.g. on modified ver-  
 211 sions of Kirchhoff’s diffraction integral (e.g. Moser & Howard, 2008; Dafni & Symes, 2017;  
 212 Yin & Nakata, 2017), specific versions of the Radon transformation and plane-wave de-  
 213 struction filters (e.g. Fomel, 2002; Karimpouli et al., 2015) or multi-dimensional stack-  
 214 ing (Dell & Gajewski, 2011; Bauer et al., 2016; Bakhtiari Rad et al., 2018). While the  
 215 latter has the advantage of being directly applicable in the time domain without the need  
 216 for specific data transformations and not requiring a detailed velocity model, the qual-  
 217 ity of the separation depends on the quality of the performed coherence measurements  
 218 and the pre-stack data.

219 A different approach to the problem was introduced by Schwarz and Gajewski (2017)  
 220 and extended by Schwarz (2019a). In contrast to previous attempts, these works specif-  
 221 ically target the reflected rather than the diffracted wavefield, with the potential ben-

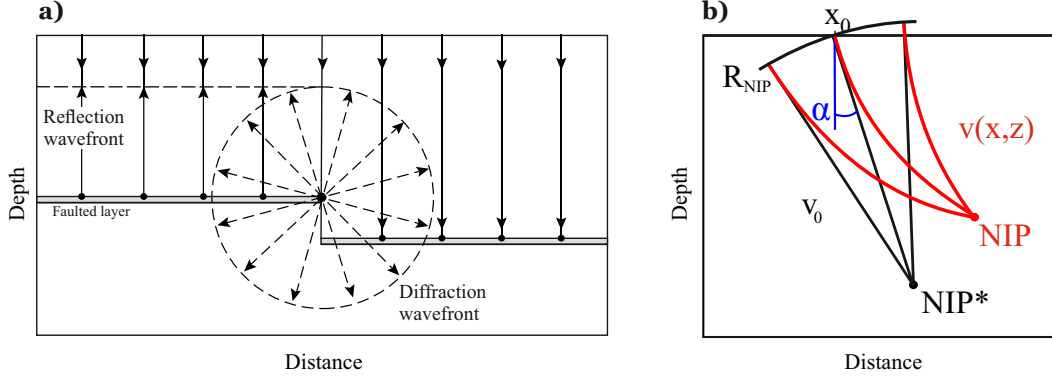


**Figure 2.** (a) Zero-Offset rays hitting a faulted layer. While reflected wavefronts obey Snell’s Law, diffracted wavefronts are scattered radially when encountering the truncated end of the faulted layer. (b) Illustration of the concept of wavefront tomography. Black lines indicate the optical image space with a medium of constant velocity  $v_0$ , in which the apparent location of the normal incidence point (NIP\*) is found by straight-ray projection. Determining the true velocity model  $v(x, z)$  and finding the true normal incidence point (NIP) location (red) is the goal of wavefront tomography.

222 efit of leaving weak diffracted signatures largely unharmed in the separated result. Like-  
 223 wise, in contrast to workflows directly incorporating Kirchhoff migration, the separation  
 224 is performed directly in the un-migrated (data) domain, leading to the applicability of  
 225 a multitude of conventional imaging and inversion algorithms. The first step of this non-  
 226 invasive strategy, very much like in surface-related multiple suppression (Verschuur et  
 227 al., 1992), constitutes in a targeted *modeling* of the interfering noise – in our case, the  
 228 reflected contributions. This is achieved by means of coherence analysis, in which the  
 229 local fit of a curved traveltime operator

$$230 \quad \Delta t(x_0, t_0) = \sqrt{\left(t_0 + 2 \frac{\sin \alpha}{v_0} \Delta x\right)^2 + \frac{2t_0 \cos^2 \alpha}{v_0} \left(\frac{\Delta x^2}{R_N} + \frac{h^2}{R_{NIP}}\right)} - t_0 \quad (1)$$

231 is optimized for neighboring traces (with midpoints laterally separated by  $\Delta x$  and half  
 232 the source-receiver distance  $h$ ), by repeatedly evaluating the semblance norm (Neidell  
 233 & Taner, 1971). Written as above, the estimated propagation time  $t_0/2$ , the emergence  
 234 angle  $\alpha$ , and the curvature radius  $R_{NIP}$  represent one-way properties of a wavefront emit-  
 235 ted by a fictitious source placed either at the normal-incidence point (NIP) or the diffrac-  
 236 tor location (compare Figure 2). While for reflections, this wavefront is fully conceptual  
 237 and expresses a symmetry in the common-midpoint gather ( $h \neq 0$ ), for diffractions  
 238 and passive events ( $R_N = R_{NIP}$ ) it describes the shape of the actual physical wavefield stem-  
 239 ming from the localized scatterer or the passive source (Bauer et al., 2017; Diekmann  
 240 et al., 2019). As a result, for reflections, sufficient offset ( $h$ ) information is needed, whereas,  
 241 for diffractions, wavefront curvatures can be fully determined in the zero-offset ( $h = 0$ )  
 242 section. Forming a by-product of coherence analysis, these wavefront attributes, in ad-  
 243 dition to velocity inversion, permit the formulation of supportive diffraction filters that  
 244 can additionally constrain the separation (Schwarz & Gajewski, 2017; Schwarz, 2019a).

245 Following this procedure of constructing a reflection model by means of local co-  
 246 herent data summations, a successful separation requires an adaptation step, which like  
 247 the summation itself should be performed within an aperture to preserve weak interfer-  
 248 ing energy. Such an adaptation of the reflection stack is achieved by introducing local  
 249 scaling coefficients  $\gamma_0$  and time shifts  $\tau_0$ . Following the superposition principle, the in-  
 250 terference of reflections and diffractions can, in good approximation be *reversed*, if the

251 estimated coherent reflection model is reasonably accurate. Expressing the coherent re-  
 252 flection stack as  $C_{ref}$ , and the raw input data as  $\mathcal{D}$ , the adaptive separation procedure  
 253 can thus be expressed as

$$254 \quad C_{diff} \approx D(x_0, t_0) - \gamma_0 C_{ref}(x_0, t_0 + \tau_0), \quad (2)$$

255 where  $(\mathbf{x}_0, t_0)$  is the central data point under consideration and  $C_{diff}$  denotes the diffracted  
 256 wavefield. For more details on the estimation of the necessary amplitude weights and time  
 257 shifts and applications in seismic and ground-penetrating-radar data, we refer to Schwarz  
 258 (2019a).

259 After their successful extraction, uncorrelated noise that was suppressed in the re-  
 260 flection model will likewise remain in the data, thereby setting natural limits on the de-  
 261 tectability of diffracted signatures. However, as diffractions, despite their weakness, pos-  
 262 sess the property of coherence, the aforementioned coherence analysis can be carried out  
 263 for the separated dataset.

## 264 4.2 Wavefront tomography

265 Based on the concept of wavefront attributes, Duvencek (2004) introduced wave-  
 266 front tomography, an efficient and robust scheme for the estimation of smooth depth-  
 267 velocity models, which has been applied successfully to industrial multi-channel data (Bauer  
 268 et al., 2017) as well as diffraction-only data (Bauer et al., 2017, 2018) and passive-seismic  
 269 measurements (Schwarz et al., 2016; Diekmann et al., 2019). In this study, due to lim-  
 270 ited offsets in the academic seismic data, the reflected measurements are hardly usable  
 271 for velocity inversion. Accordingly, wavefront attributes have to be extracted from the  
 272 diffraction-only data  $C_{diff}$  obtained during the previous step. This is done by means of  
 273 coherence analysis, during which the hyperbolic travelttime moveout approximation (1)  
 274 is locally fitted to the data (e.g. Jäger et al., 2001). The input for wavefront tomogra-  
 275 phy consists of numerous sets of wavefront attributes that can be picked in an automatic  
 276 fashion in the resulting zero-offset sections based on their coherence,

$$277 \quad \mathbf{d}_i = (\xi, T, \alpha, R_{NIP})_i, \quad \text{with } i = 1, \dots, n_{picks}, \quad (3)$$

278 where  $n_{picks}$  denotes the total number of picked data points,  $T = t_0/2$  the one-way zero-  
 279 offset travelttime and  $\xi$  the position on the recording surface. The model parameters  $\mathbf{m}$   
 280 are the B-spline velocity coefficients  $v(x, z)$  on a pre-defined grid of  $n_x \times n_z$  knots and  
 281 localizations  $(x, z)_i$  and ray-takeoff angles  $\theta_i$  associated with each data point. The ini-  
 282 tial localizations and ray-takeoff angles are obtained by downward kinematic ray trac-  
 283 ing into the initial model (which in our applications merely consists of the constant near-  
 284 surface velocity  $v_0$ , compare Figure 2b) starting from  $\xi_i$  under the angles  $\alpha_i$  until the  
 285 remaining travelttime vanishes. Subsequently, upwards dynamic ray tracing from  $(x, z, \theta)_i$   
 286 yields the modelled data points  $\tilde{\mathbf{d}}$ . The misfit between the measured and modelled data  
 287 points  $\Delta \mathbf{d} = \mathbf{d} - \tilde{\mathbf{d}}$  defines the cost function,

$$288 \quad \Psi(\mathbf{m}) = \frac{1}{2} \|\mathbf{d} - \tilde{\mathbf{d}}\|_2^2 + \Lambda(\partial_{xx}v(x, z), \partial_{zz}v(x, z)), \quad (4)$$

289 where  $\Lambda$  constitutes a regularisation term that ensures a smooth velocity model. Dur-  
 290 ing the inversion, the cost function is minimized iteratively in a damped-weighted least-  
 291 squares sense until a velocity model and localizations  $(x, z)_i$  are found that are most con-  
 292 sistent with the measured wavefront attributes (compare Figure 2b). For stability, we  
 293 apply the inversion algorithm in a cascaded fashion, starting from a coarse grid and then  
 294 successively increasing the number of B-spline knots.

## 295 5 Data-driven results

### 296 5.1 Diffraction separation

297 In order to reveal the faint diffracted wavefield, we perform diffraction separation  
 298 based on the approach by Schwarz (2019a). As input, we use the CMP stack of seismic

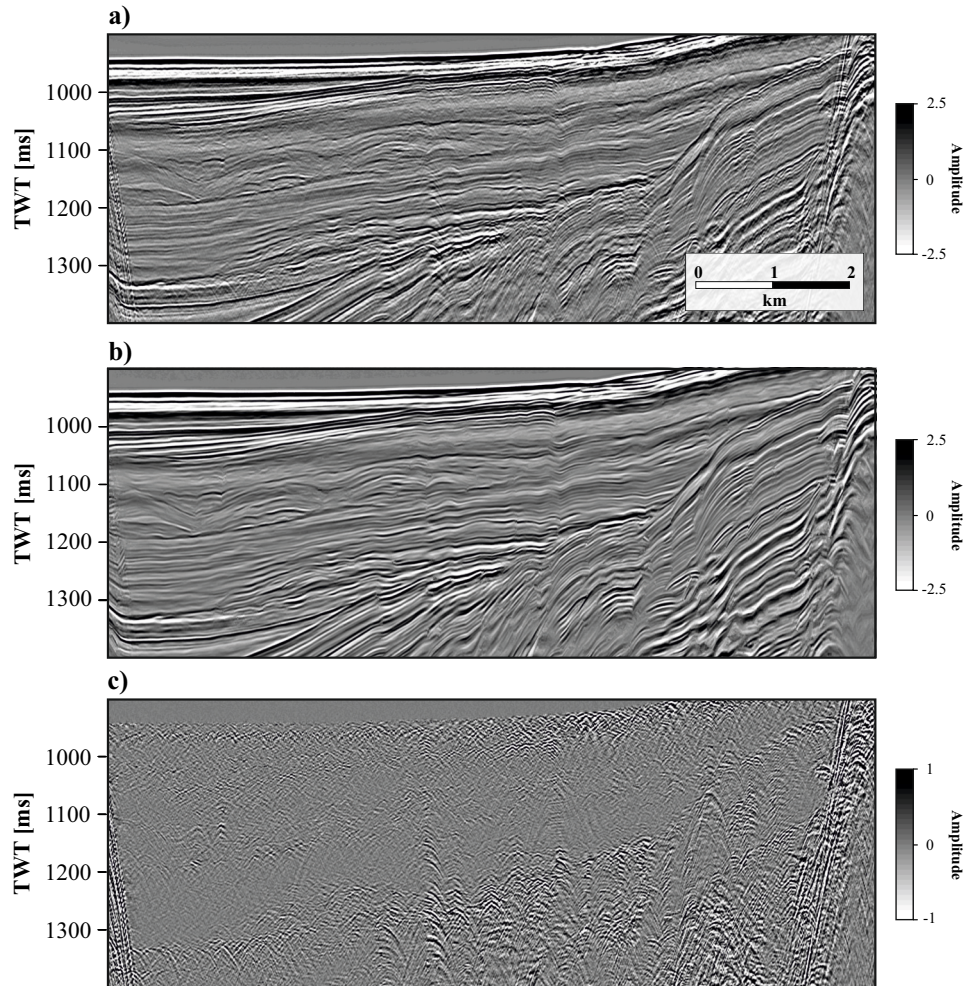


**Figure 3.** Results of the coherent stacking and subtraction scheme for diffraction separation illustrated on a zoomed section from seismic line 11: (a) the input CMP Stack, (b) the reflection-only data and (c) the diffraction-only data.

line 11 with a CMP-spacing of 12.5 m from the POS338 data-set (Figure 1 and Figure 3a). With the purpose of recovering as much of the diffracted wavefield as possible, preprocessing for the separation was kept to a minimum comprising only simple bandpass filtering for the removal of low-frequent swell noise, SRME for multiple elimination in addition to the application of a top mute and trace mute. The processing flow is illustrated in Figure S1.

In the first step, we carry out coherent wavefield summation using planar beam-forming in order to estimate the reflection-only data. With a lateral aperture of 100 m and a coherence time window of 20 ms, supported by a wavefront filter with a maximum angle of  $10^\circ$  to search for, we obtain the reflection-only section illustrated in Figure 3b. As demonstrated by Schwarz (2019a), the lateral aperture plays an important role in the success of the modeling of the reflected wavefield as it controls the number of traces used for the coherent stacking and, consequently, how discriminative the separation is. The more traces are considered, the more of the crossing diffraction energy is neglected in the reflection-only data, and the better the diffraction-subtraction works later on. However, as too large apertures tend to smear the reflections, the proper aperture choice can be seen as a trade-off and, consequently, requires parameter testing (Schwarz, 2019a). As Figure 3b demonstrates, the reflection-only section has a higher lateral continuity compared to the input CMP stack (Figure 3a) and, more importantly, is free of diffractions.

In the next step, the diffraction-only data is generated by performing coherent beam subtraction. Also here, the lateral aperture is an important parameter and several tests showed that using 400 m is the best trade-off value. An example of the effect of different apertures used for the separation is given in the supplementary information (Figure S2). The resulting diffraction-only section is illustrated in Figure 3c. This section is generally free of reflections and a rich, complex diffracted wavefield is revealed. Diffractions can be identified throughout the section, but seem to cluster around distinctive structures. Not only vertical structures that seem to represent faults but also horizontal structures that seem to represent unconformities are highly *diffractive*. Note e.g. the high number of diffractions along the faults in the center of the basin and towards the marginal Astypalaea fault. This illustration highlights that most of the diffractions at faults are created at the tips of the faulted horizons. Consequently, faults seem only diffractive when reflection-horizons are present.

The numerical cost of the whole diffraction separation routine can be considered as fairly reasonable. The seismic line under consideration comprises 2022 CMPs and was acquired with a sampling rate of 1 ms and a recording length of 3 s. On a conventional computer with a quad-core processor, the coherence analysis for deriving the reflection-only data took approx. 10 minutes and the adaptive subtraction for generating the diffraction-only data approx. one hour.

## 5.2 Wavefront tomography

In order to derive a depth-velocity model, we apply the previously introduced wavefront-tomographic scheme based on the separated zero-offset diffraction response. In the first step, we estimate the wavefront attributes and the diffraction coherence using the semblance norm. Figure 4a illustrates the resulting semblance section overlain by 11,866 automatically picked data points, which consist of sets of wavefront attributes that form the input of the inversion algorithm. These data points are scattered over the whole section ensuring the needed illumination for velocity inversion. In order to avoid contributions from the faint multiple remnants, we mute the diffraction coherence below the arrival time of the seafloor multiple before the automatic picking. In the next step, we calculate the initial model without assuming any a priori information other than the near-surface velocity  $v_0 = 1.52$  km/s which corresponds to the regional water velocity. The resulting initial model is displayed in Figure 4b together with the initial ray starting locations associated with each data point, which are obtained by downward kinematic ray tracing into the constant initial model. During the inversion, we applied two grid refine-

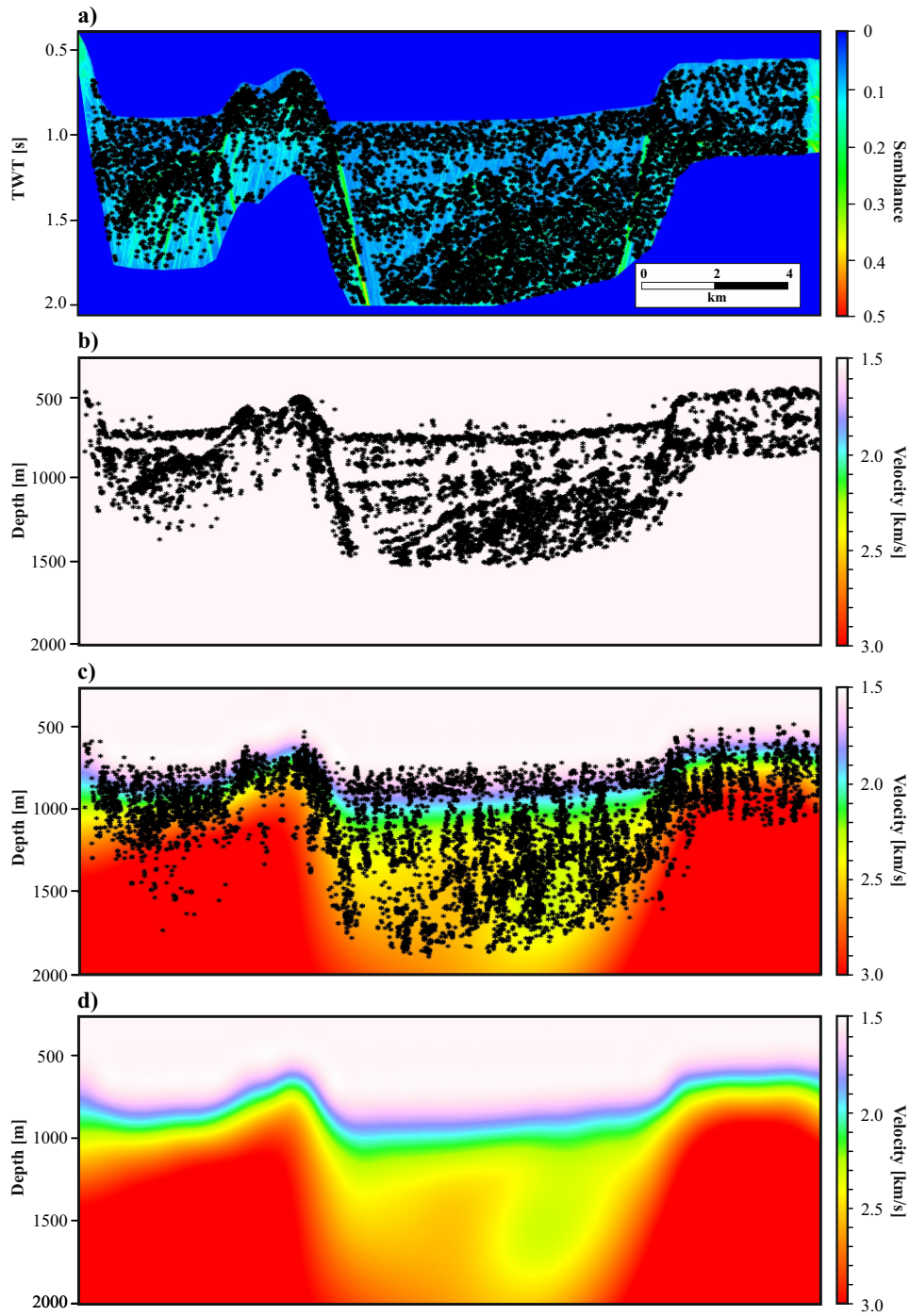


**Figure 4.** Results of diffraction-based wavefront tomography. (a) All 11,866 automatically picked data points plotted into the semblance section. (b) The constant initial model for the inversion overlain by the initial scatterer localizations. (c) Final velocity model overlain with final scatterer localizations. (d) Final velocity model.

ments, the first nine iterations with  $11 \times 5$  B-spline knots and a spacing of 2500 m in  $x$ - and 625 m in  $z$ -direction, followed by eight iterations with  $21 \times 9$  B-spline knots (1250 m in  $x$ - and 312.5 m in  $z$ -direction) and seven iterations with  $41 \times 17$  B-spline knots (625 m in  $x$ - and 156.25 m in  $z$ -direction). The resulting velocity model overlain with the final scatterer locations after a total of 24 iterations is illustrated in Figure 4c. While the scatterer locations were distributed quite broadly in the semblance section, the final scatterer locations seem to be more focussed after the inversion. We identify several areas where the final scatterer locations organize in vertical structures following the outline of faults.

Figure 4d shows the velocity distribution inferred from the diffracted wavefield. The inverted velocities range between from 1.5 km/s to 3.0 km/s. The basement is estimated at approx. 3.0 km/s while for the sedimentary strata a rather smooth velocity increase from 1.5 km/s to approx. 2.5 km/s has been inverted. In general, the velocity model acknowledges the expected velocity contrast from the sedimentary strata to the basement very well. Especially the elevated basement of the Anhydros Horst is distinctly expressed in the velocity model. The velocity distribution in the Santorini-Anafi basin is characterized by a lateral velocity increase between the left and the right part of the basin. While the inverted velocities in the right part do not exceed 2.5 km/s, high velocities of over 2.9 km/s can be found within the sedimentary strata of the left part of the basin. In contrast to that, the velocity distribution for the Astypalaea plateau and the Amorgos basin show no comparable lateral velocity variations.

### 5.3 Depth imaging

In the next step, we use the data-derived velocity model for finite-difference depth migration. As input for the migration, we use the zero-offset section after multiple elimination which has also been used as input for diffraction separation (see Figure S1). The result is displayed in Figure 6a. In general, the quality of the depth image seems good as most faults are sharply focussed and there are no obvious artifacts. Also the rugged basement reflection is well imaged and all of its many edges are sharply focused. While the margins of the Santorini-Anafi basin are reconstructed reasonably well, we observe a slight down-bending of the seafloor-reflections towards the Anhydros horst and the Astypalaea plateau which could be explained as a consequence of the smoothness of the velocity model.

In addition, we present a diffraction depth image of the profile obtained by means of finite-difference migration of the diffraction-only data using the inverted velocity model. By calculating the squared envelope of the migrated diffractions, we arrive at an image that illustrates the *diffraction energy* (Figure 4b). Such a diffraction depth image provides highly-resolved structural detail. In particular, it highlights the complex system of internal faults in the center of the Santorini-Anafi basin and on the Astypalaea plateau. These faults are expressed as linear, slightly curved features and can be traced nicely through the seismic section and seem to penetrate the seafloor on the Astypalaea plateau. Furthermore, we observe that the Anhydros horst is associated with a high degree of diffractivity, possibly as a consequence of tectonic exposure or erosion. Interestingly, some unconformities can be clearly delineated in the diffraction image, while others are expressed as faint or even transparent events which suggests a different roughness associated with these horizons.

## 6 Interpretation-driven refinement

### 6.1 Quality Control

As mentioned in the previous section, the data-derived velocity model presented in Figure 4d depicts the expected velocity distribution of the profile quite well. The sedimentary strata is generally associated with a rather gentle velocity increase from ap-

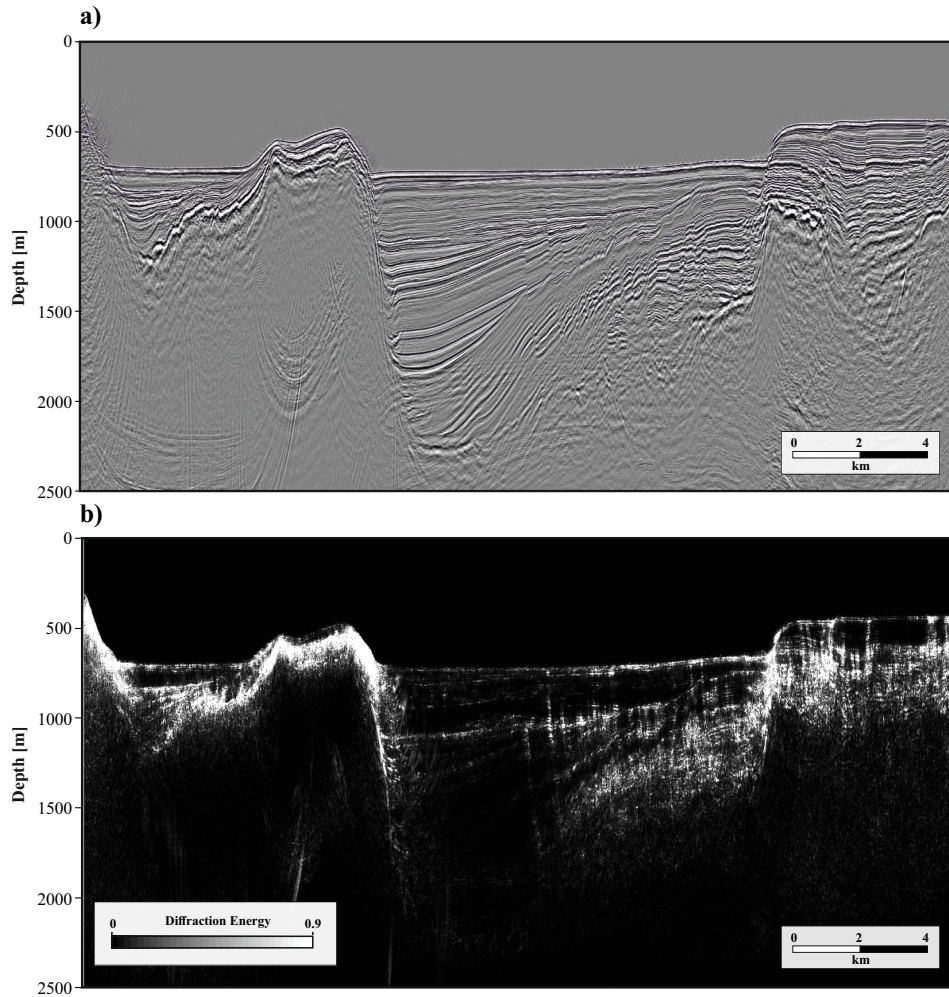


**Figure 5.** (a) Finite-differences depth migration of the full wavefield using the velocity model illustrated in Figure 4d. (b) Diffraction energy calculated from the finite-differences depth-migrated diffraction-only data using the inverted velocity model illustrated in Figure 4d.

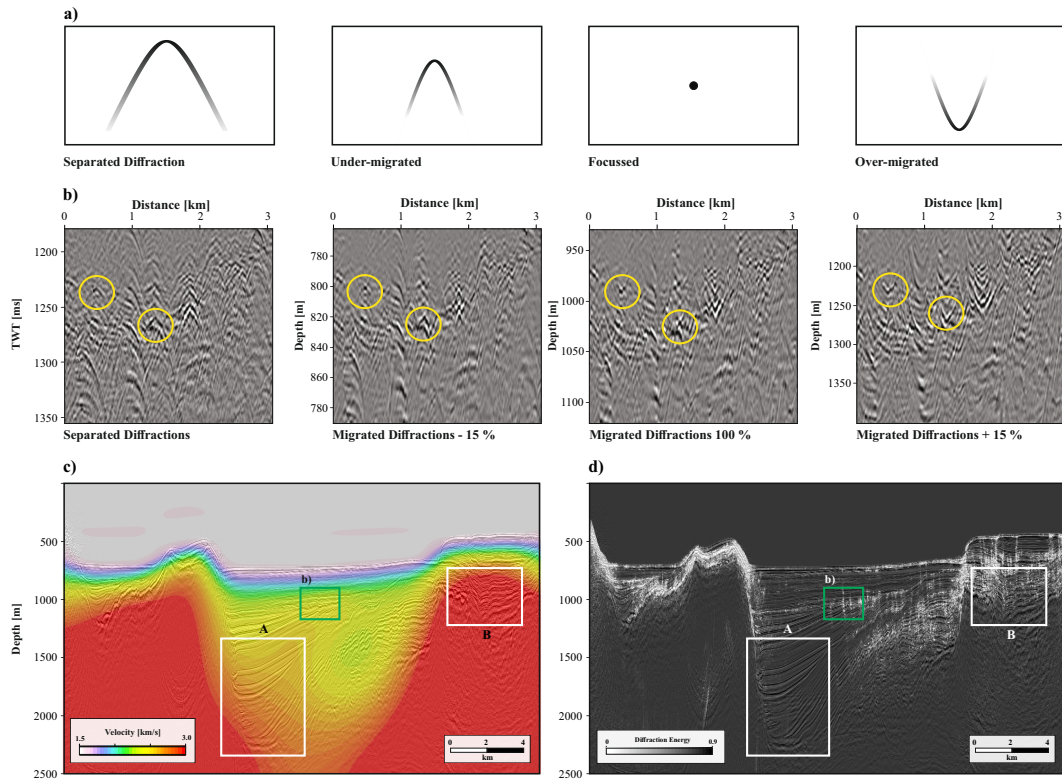


**Figure 6.** (a) Schematic illustration of how migration with different velocities affects the shape of diffractions. (b) A small excerpt of the seismic section after diffraction separation. Migration with different velocities results in under-migration (-15%), focusing (100%) or over-migration (+15%). Two prominent instances are highlighted by the yellow circles. (c) Finite difference migrated seismic section overlain with the inverted velocity model and (d) the diffraction depth image. White rectangles indicate areas of unexpected high velocities within the sedimentary strata. The green rectangle indicates the location of the small excerpt shown in (b).

402 prox. 1.5 km/s to 2.5 km/s while the basement is associated with higher velocities in the  
 403 order of 3.0 km/s. These values are mostly in agreement with the regional tomographic  
 404 model presented by Heath et al. (2019), who attribute metamorphic basement and sed-  
 405 imentary strata with to velocities higher or lower than 3.0 km/s, respectively (compare  
 406 their Figure 5). However, a more detailed comparison of their results is not feasible as  
 407 the presented velocity models are too coarsely resolved considering the high complex-  
 408 ity of the data under consideration.

409 In order to further assess the quality of our velocity model, we (i) analyze the fo-  
 410 cusing of diffractions after migration and (ii) evaluate the geological plausibility of the  
 411 inverted velocities. In a similar way to the velocity analysis of conventional long-offset  
 412 data, where the flatness of common-image-gathers (CIG) is used for quality control, we  
 413 assess the focusing behavior of diffractions to evaluate the quality of the velocity model.  
 414 Figure 6a shows a schematic illustration of how diffractions appear after the migration  
 415 with different velocities. If too low velocities are used, the diffractions will be under-migrated  
 416 and have downwards-bent tails. If the velocity used for the migration is correct, the diffrac-  
 417 tions will be focussed. Using too high a velocity results in over-migration and upwards-  
 418 bent diffraction tails.

419 Following this strategy, we evaluated the behavior of the separated diffractions af-  
 420 ter migration with the inverted velocity model with velocity models perturbed by  $\pm 15\%$ ,  
 421 respectively. An excerpt from the result containing numerous diffractions is illustrated  
 422 in Figure 6b (see Figure 6c for the location within the profile). Two prominent instances  
 423 are emphasized by the yellow circles. Migrating the separated diffractions with a veloc-  
 424 ity model of  $-15\%$  of the inverted velocity model leads to a narrowing of the diffraction  
 425 tails but they remain visible in the section. In contrast to that, the migration of the diffrac-  
 426 tions with the inverted velocity model leads to an overall focusing and the section ap-  
 427 pears generally free of diffraction tails. The migration with  $+15\%$  leads to an over-migration  
 428 of the diffractions and we can identify numerous upwards-bent diffraction tails within  
 429 the seismic section. These observations show that the inverted velocity model fits the  
 430 data quite well and can be validated at least with an approximate confidence interval  
 431 of  $\pm 15\%$ .

432 By applying this quality control procedure throughout the seismic section, we were  
 433 able to validate the inverted velocities for most of those areas, in which distinct diffrac-  
 434 tions are present e.g. along faults. In areas where the diffracted wavefield is more com-  
 435 plex, however, focussing is more complicated to assess quantitatively. Especially in the  
 436 vicinity of the alpine basement, we can not be certain that we take only point diffrac-  
 437 tions into account as we might encounter lenticular objects (Malehmir et al., 2009). In  
 438 addition, the focusing of diffractions is only an appropriate quality control tool if scat-  
 439 tering occurs in or close to the acquisition plane. However, in case of out-of-plane scat-  
 440 tering, diffraction focusing is not an appropriate measure for quality control. As such  
 441 diffractions appear with distorted curvatures, they will also affect the quality of the ve-  
 442 locity inversion. As shown by Malehmir et al. (2009), such out-of-plane diffractions can  
 443 contribute from considerable distances from the acquisition plane. The identification of  
 444 out-of-plane contributions still constitutes a challenge and we have to assume that our  
 445 estimates are affected by them. We argue, however, that the inverted velocities from the  
 446 diffracted wavefield can be expected to be reliable when a high density of diffractions e.g.  
 447 from elongated faults are encountered. It is reasonable to assume that such structures  
 448 are most likely to be located in the acquisition-plane and, consequently, diffraction fo-  
 449 cusing can be used for quality control in these areas. In contrast, inverted velocities in  
 450 areas that are constrained by few events should be assessed with caution.

451 Therefore, we use a second criterion for evaluating the quality of the inverted ve-  
 452 locity model: the geological plausibility. Figure 6c illustrates the depth-migrated section  
 453 overlain with the inverted velocity model and Figure 6d shows the depth-migrated sec-  
 454 tion overlain with the diffraction depth image. We observe considerable lateral velocity  
 455 variation within the Santorini-Anafi basin. In the right part of the basin, the velocities  
 456 of the sedimentary strata are generally lower than 2.5 km/s while in the left part of the

457 basin, we observe a zone with high velocities exceeding 2.9 km/s as highlighted by Rect-  
 458 angle A. Those velocities can be considered geologically implausible for the expected ma-  
 459 rine sediments (Nomikou et al., 2018). As can be seen in Figure 6d, this area is mostly  
 460 free of diffraction events. This lack of illumination might explain why implausibly high  
 461 velocities have been inverted here. If an area is not properly constrained by diffractions,  
 462 the inverted velocity model is more likely to suffer from interpolation artifacts or wrongly-  
 463 fitted events. However, the right part of the basin is characterized by a high degree of  
 464 diffractivity, which makes the respective velocity better supported by data.

465 Furthermore, Rectangle B highlights an area with high velocities in the center of  
 466 the Astypalaea plateau. Here, the contact of the basement and the sediments is not prop-  
 467 erly acknowledged by the inverted velocity model and the lower sedimentary strata are  
 468 associated with velocities of approx. 3.0 km/s, which, again, seems not plausible here.  
 469 The margins of the plateau, however, are associated with lower velocities and honor the  
 470 contact of the basement and the sediments more accurately. In contrast to the region  
 471 denoted by Rectangle A, Figure 6d indicates that the area within Rectangle B is actu-  
 472 ally constrained by numerous diffractions. However, we know from Nomikou et al. (2018)  
 473 that the Astypalaea plateau is a complex region with a highly varying sedimentary thick-  
 474 ness and a very rugged basement. Therefore, the probability of out-of-plane contribu-  
 475 tions is high in this area, which could explain why unrealistically high velocities have been  
 476 inferred.

477 These observations highlight the two main limitations of the proposed velocity in-  
 478 version workflow for 2D seismic acquisitions: the lack of diffractions in some regions and  
 479 out-of-plane contribution. However, if 3D data are considered, the problem of out-of-plane  
 480 can be addressed (e.g. Bauer et al., 2020). Other limitations of the data-driven veloc-  
 481 ity estimation are the fact that it does not account for anisotropy and that smoothing  
 482 does not account for the strong velocity contrasts e.g. at the contact of the basement  
 483 and the sedimentary strata. This could explain e.g. the previously mentioned down-bending  
 484 of the seafloor reflection close to the Anhydros horst in the migrated section (Figure 5a).

## 485 6.2 Velocity model refinement

486 Although our quality control showed that the data-derived velocity model is reli-  
 487 able in extended regions, in certain areas the velocities are implausible for the previously  
 488 explained reasons. In order to derive a velocity model that is geologically consistent through-  
 489 out, we suggest an interpretation-driven refinement that utilizes the strengths of the data-  
 490 driven velocity inversion to compensate for its weaknesses.

491 Therefore, our strategy is to extract 1D velocity profiles for every 100th CMP from  
 492 the inverted velocity model and to assign the extracted velocities to stratigraphic units.  
 493 This procedure is illustrated in Figures 7a and b. The dashed rectangles highlight those  
 494 areas, where our quality control indicated zones of implausible velocities. For each layer,  
 495 we estimate the average value of the extracted velocity and round this estimate to the  
 496 second decimal place. Afterwards we correlate the units within each compartment of the  
 497 seismic profile and determine a mean value for the respective stratigraphic layer, while  
 498 excluding all values within the pre-defined zones of uncertainty. The resulting correlated  
 499 units for each compartment are illustrated in Figure 7b.

500 In the next step, we assemble a velocity model for the whole seismic section based  
 501 on the correlated units. The resulting model is depicted in Figure 7c. Apart from the  
 502 zones of high uncertainty, the resulting velocity model is comparable to the original data-  
 503 driven inversion. For each compartment, the refined velocity model fits the stratigraphic  
 504 interpretation by Nomikou et al. (2018) reasonably well. In general, the velocity model  
 505 consists of an upper layer with rather low-velocities of approx. 1.6 - 1.7 km/s underlain  
 506 by a layer with an interval velocity of approx. 1.8 km/s. Below these upper units, we iden-  
 507 tify several intermediate units with velocities in the order of 2.0 - 2.2 km/s which are com-  
 508 parably thin for most parts of the profile but have a large thickness in the Santorini-Anafi  
 509 basin. The lowermost units comprise velocities of approx. 2.4 km/s. Although a com-  
 510 parison is only partially feasible, this refined velocity model is in general agreement with

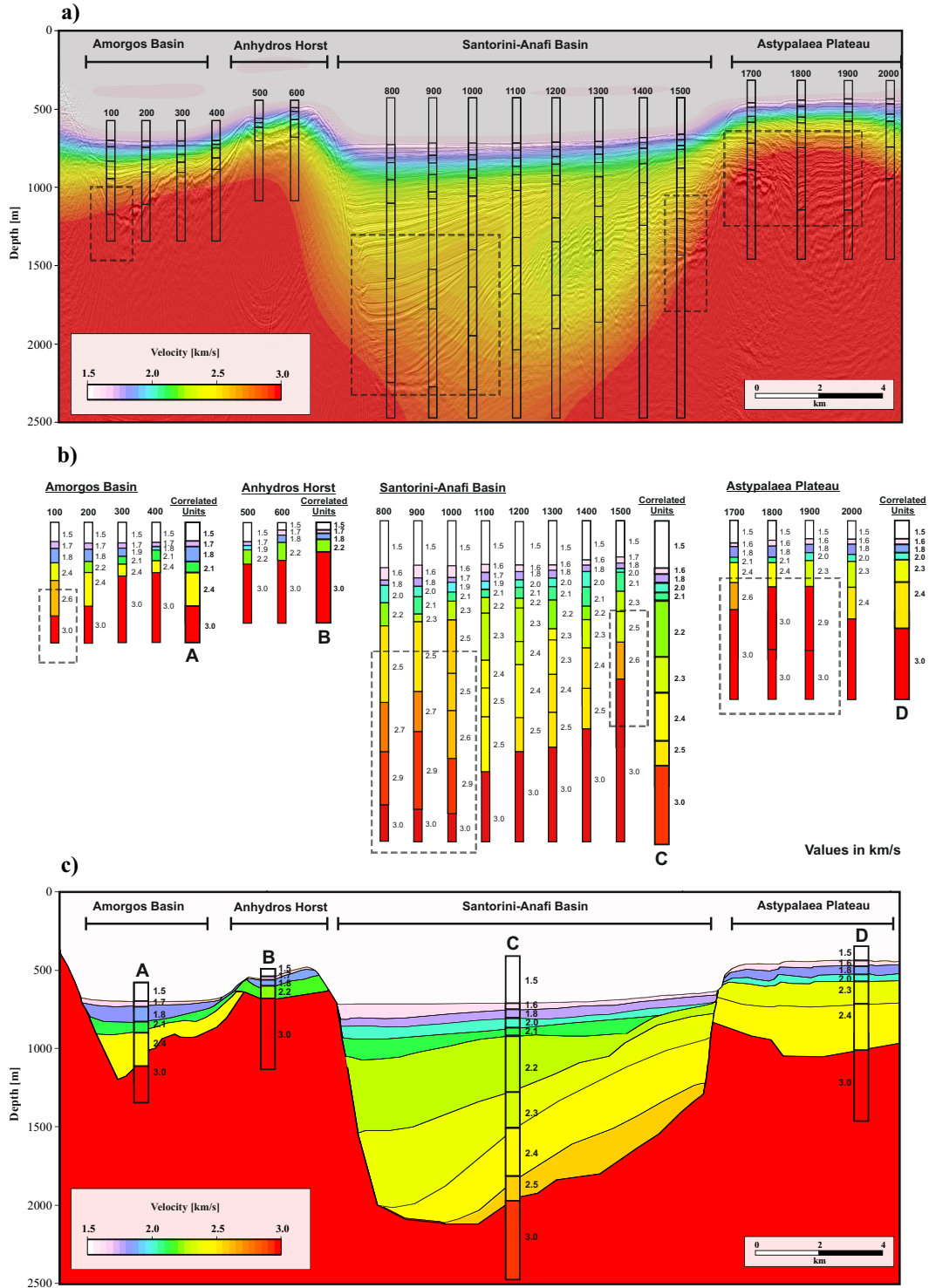


**Figure 7.** Illustration of the interpretation-driven velocity refinement. (a) Finite difference migrated seismic section overlain with the inverted velocity model and our sampling points. (b) Extracted velocity values for each stratigraphic layer and the correlated units. The dashed rectangles highlight those areas where our quality control indicated implausible velocities. (c) Refined velocity model.

511 the regional tomographic model presented by Heath et al. (2019) while remaining ge-  
 512 ologically plausible. However, just like any other means of interpretation, the whole re-  
 513 finement process is subject to a certain degree of subjectivity and does not account for  
 514 lateral velocity variations within the compartments of the seismic section e.g. as a re-  
 515 sult of compaction. It might be stressed at this point that the proposed interpretational  
 516 guide is informed by the lateral continuity of the reflected wavefield, which emphasizes  
 517 the distinct yet complementary nature and synergetic potential of reflections and diffrac-  
 518 tions for imaging.

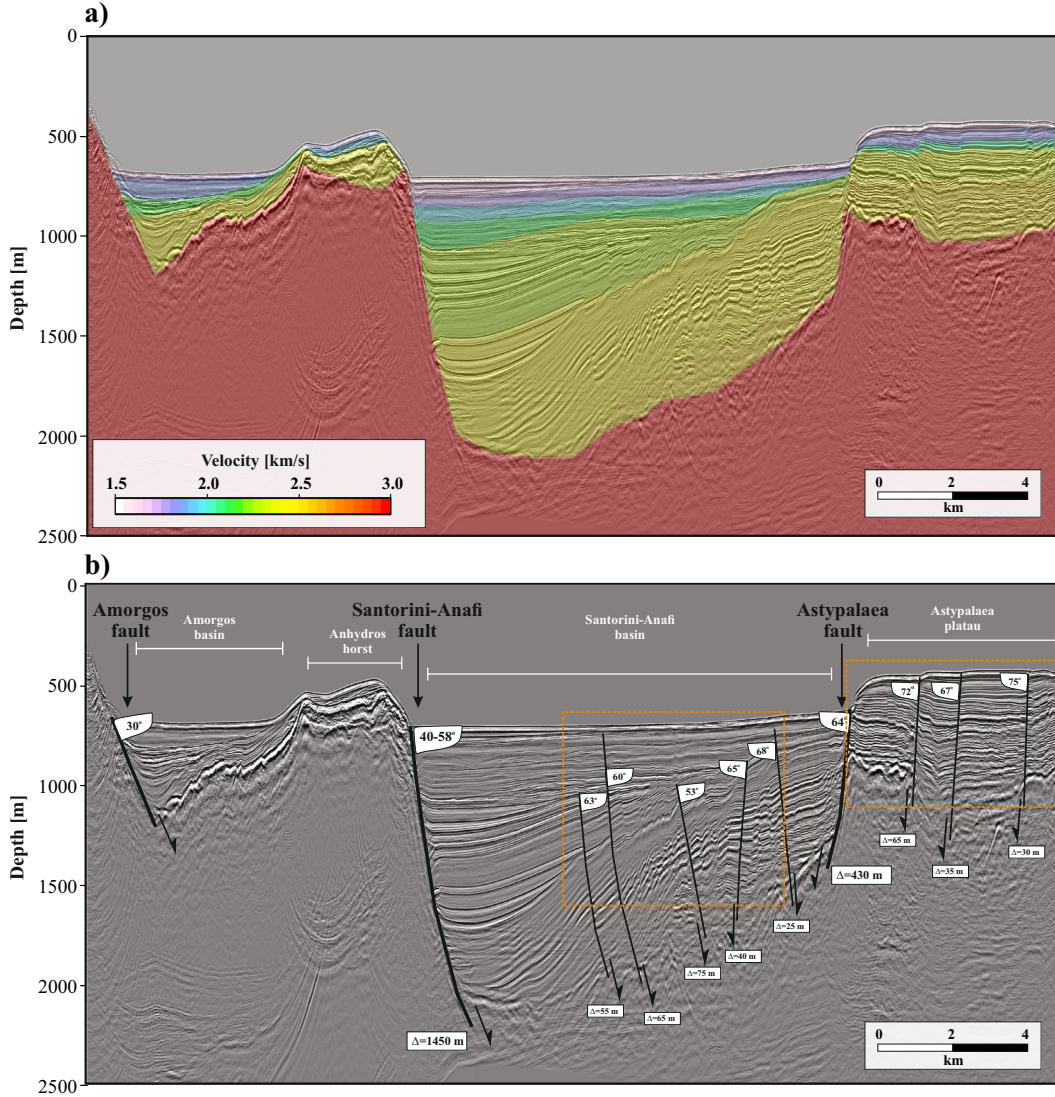


**Figure 8.** (a) Full-wavefield depth image superimposed by refined velocity model used for migration. (b) Depth image as in (a) but shown with dipping angles and throws estimated for the most prominent faults. Orange rectangles announce two sections that are highlighted in Figure 9.

### 519 6.3 Geological implications

520 Figure 8a shows the finite-difference depth-migrated seismic section overlain with  
 521 the refined velocity model. This illustration highlights the geological plausibility of the  
 522 velocity model. Since the refined velocity model takes into account the high velocity con-

523 trast between the metamorphic basement and the sedimentary strata, the depth-migrated  
 524 image is now free of artifacts such as the warping of the seafloor reflection, which had  
 525 been observed after the migration with the data-driven velocity model (Figure 5a). The  
 526 overlay of the velocity model and the seismic section further suggests a stratigraphic re-  
 527 lationship of the lowermost units of the Amorgos basin, the Santorini-Anafi basin, and  
 528 the Astypalaea Plateau.

529 Figure 8b illustrates the refined finite-difference depth-migrated image as well as  
 530 the dipping angles and throws of the most significant faults. Based on this depth image,  
 531 we infer the total thickness of the sedimentary strata to be approx. 1.4 km, which is re-  
 532 markable considering that the marine sediments of the SATZ are considered to be of Plio-  
 533 Quaternary age (Perissoratis, 1995). In order to understand the acting forces responsi-  
 534 ble for the formation and the evolutionary history of this rift-zone, it would be very help-  
 535 ful to estimate the amount of extension. Having derived a depth-converted seismic sec-  
 536 tion, we encourage the application of structural restoration (Nunns, 1991) in future stud-  
 537 ies in order to reconstruct and measure the extension in the Santorini-Anafi basin.

538 Using the interpretation-software KINGDOM, we measure the angles and throws  
 539 of the most significant faults as illustrated in Figure 8b. Compared to the estimates by  
 540 Nomikou et al. (2018), our study indicates smaller angles for the marginal Amorgos-fault  
 541 ( $30^\circ$  compared to  $38^\circ$ ) and the listric Santorini-Anafi fault ( $40\text{--}58^\circ$  compared to  $68^\circ$ )  
 542 and a larger angle for the Astypalaea fault ( $64^\circ$  compared to  $45^\circ$ ) but still indicate nor-  
 543 mal faulting to be the main tectonic mechanism responsible for basin formation. While  
 544 the throw of the marginal faults is very significant (approx. 1450 m for the Santorini-  
 545 Anafi fault and approx. 430 m for the Astypalaea fault), the throw of the most impor-  
 546 tant internal faults ranges from 25 to 75 m. Their fault angles lie between  $53^\circ$  and  $75^\circ$ .  
 547 As indicated in Figure 8b, the sense of displacement of the internal faults within the cen-  
 548 ter of the Santorini-Anafi basin changes from NW to the SE forming narrow subsided  
 549 zones in the center. In order to further analyze the internal fault systems, we utilize the  
 550 diffraction depth image derived with the refined velocity model. As shown in Figure 5b,  
 551 such diffraction images highlight small-scale heterogeneity and seem to be good indica-  
 552 tors for faulting, tectonic overprint or erosion.

553 As already mentioned by Schwarz (2019a), diffraction images are highly suitable  
 554 to be used as an alternative to conventional attributes for fault interpretation as e.g. im-  
 555 age coherence or image curvature (Bahorich & Farmer, 1995; Marfurt et al., 1998; Chopra  
 556 & Marfurt, 2007). Following this notion, we combine the diffraction depth images and  
 557 the refined depth images to arrive at physically informed laterally resolved discontinu-  
 558 ity maps. Two examples of these maps are illustrated in Figure 9 for the Astypalaea plateau  
 559 (a-c) and the intrabasinal fault system of the Santorini-Anafi basin (d-f). By blending  
 560 the diffraction image with the depth-migrated images, we are able to combine the strengths  
 561 of both the reflected and the diffracted wavefield to facilitate the identification of faults.  
 562 Especially when considering highly complex fault systems such as the the intrabasinal  
 563 faults in the Santorini-Anafi basin (Figure 9d-f), the diffraction maps provide a power-  
 564 ful guide for the systematic delineation of individual faults.

565 Based on these images we present a sketch of the outline of the identified fault sys-  
 566 tems on the Astypalaea plateau (Figure 9c) and in the Santorini-Anafi basin (Figure 9f).  
 567 In both sections, we identify zones in which the sense of displacement of the faults changes  
 568 from the NW to the SE forming narrow subsided zones in the center (see arrows in Fig-  
 569 ure 9c and f). On the one hand, these subsidiary faults could be interpreted as forming  
 570 a part of negative flower structures. Such negative flower structures would be an indi-  
 571 cation for some form of strike-slip movement (Harding, 1990). On the other hand, the  
 572 shape of the subsidiary faults could also be explained as the result of antithetic fault-  
 573 ing with respect to the marginal Santorini-Anafi fault. In order to further analyze these  
 574 narrow zones, however, adjacent seismic lines need to be considered. It is interesting that  
 575 faulting within the Santorini-Anafi basin is mostly restricted to the strata below the un-  
 576 conformity highlighted by the dashed line in Figure 9f. This is clearly visible both in the  
 577 presented diffraction images (Figure 5b) and the fault image (Figure 9e). Only a few faults

578 penetrate the strata above and their displacement is significantly smaller above than be-  
 579 low this unconformity (several meters vs. several tens of meters). This indicates that this  
 580 unconformity marks a significant change in the tectonic behavior of the fault system. Ei-  
 581 ther the internal faulting within the Santorini-Anafi basin has ceased mostly after the  
 582 formation of this unconformity or the deposition of the upper units has happened very  
 583 rapidly with regard to the rate of faulting.

584 In order to further investigate the timing, orientation, and nature of the identified  
 585 faults, however, adjacent profiles from the POS338 data-set have to be taken into account.  
 586 The internal consistency of the presented results suggests that the proposed diffraction-  
 587 based workflow for depth imaging is practically feasible and its application to other pro-  
 588 files recorded in the working area is strongly recommended. It was demonstrated that  
 589 no offset information is required, which makes the vast range of vintage seismic profiles  
 590 from the SATZ new candidates for resolving the debate on strike-slip deformation in the  
 591 SATZ shedding new light on the volcano-tectonic evolution of this remarkable morpho-  
 592 tectonic zone.

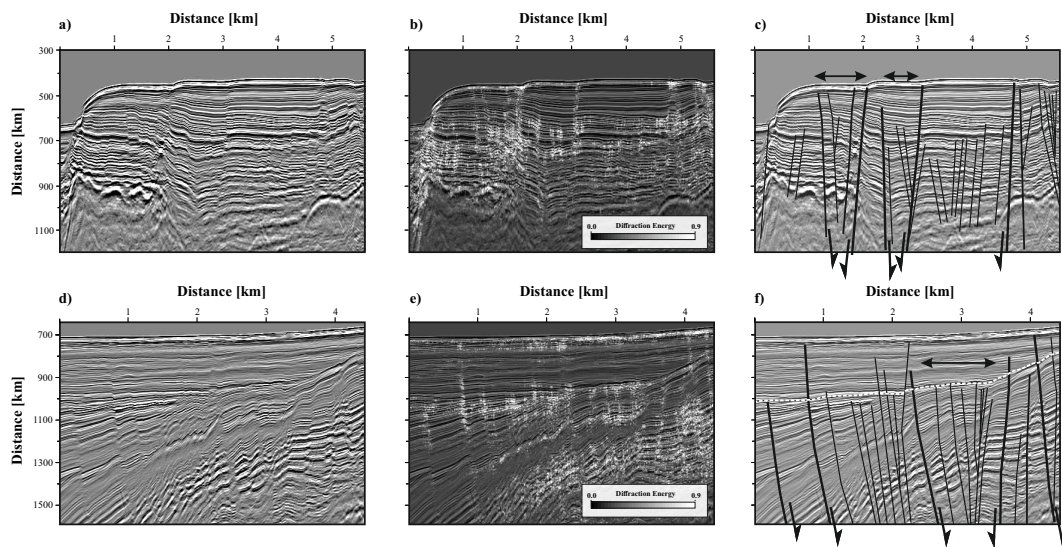


**Figure 9.** Excerpts of the final depth image of the Astypalaea plateau and the Santorini-Anafi basin (a,d), the respective fault attribute maps (b,e) and the corresponding fault interpretation (c,f). For location see Figure 8b.

## 593 7 Conclusions and Outlook

594 In this study, we have shown how the diffracted wavefield can be utilized to enable  
 595 depth-conversion of academic seismic data without the need for offset information. Us-  
 596 ing an offset-limited academic seismic line from the Santorini-Amorgos Tectonic Zone  
 597 (SATZ), we reveal a rich diffracted wavefield by means of a robust separation scheme that  
 598 models and adaptively subtracts the reflected wavefield from the data. We use the sepa-  
 599 rated diffractions to estimate insightful wavefront attributes and perform wavefront to-  
 600 mography to, for the first time in the study area, derive a depth-velocity model which  
 601 we use for finite difference depth migration. The diffraction-based velocity model reli-  
 602 ably honors the most prominent features of the seismic profile and accounts for the ex-  
 603 pected sudden velocity increase at the sediment-basement interface.

604 We further analyze the quality of the inverted velocity model by examining the fo-  
 605 cusing of diffractions in a similar manner as common-image-gathers are used in reflection-  
 606 based processing. Founded on this quality-control scheme, we show that the inverted ve-

607 locality model is reliable where distinct diffractions from elongated faults are considered  
 608 as these structures are most likely to lie within the acquisition plane. Here, we were able  
 609 to validate the inverted velocities at least with an approximate confidence interval of  $\pm$   
 610 15% which we consider acceptable in the context of low-budget academic data. Due to  
 611 the effect of possible out-of-plane contributions and the partial absence of illumination,  
 612 however, we identify some areas of the inverted model with geologically implausible ve-  
 613 locities. Based on the partial lateral continuity of reflection events, we suggest a com-  
 614plementary knowledge-guided refinement that remains geologically plausible across the  
 615 full investigated study area.

616 In addition, we also perform a depth migration of the separated diffracted wave-  
 617 field to derive spatial diffraction images. These highly resolved reconstructions provide  
 618 detailed insight into processes like erosion (diffraction at unconformities) or tectonic over-  
 619 print (diffraction at faults). Following the notion of using the diffraction images as phys-  
 620 ical attribute maps, a combination with full-wavefield depth images is demonstrated to  
 621 facilitate the identification of faults and other discontinuous features in depth. Led by  
 622 these findings, we encourage using the diffracted wavefield for the direct imaging of com-  
 623 plicated fault and fracture systems in depth.

624 The presented depth image allows the first data-based quantification of the thick-  
 625 ness distribution of the sedimentary strata as well as fault angles and throws within the  
 626 SATZ. We estimate a maximum sedimentary thickness of approx. 1400 m and angles of  
 627 the marginal faults that indicate normal faulting. Several narrow fault systems identi-  
 628 fied by means of the unique diffraction depth images in the Santorini-Anafi basin and  
 629 on the Astypalaea plateau appear to be of flower-like assembly. We hypothesize that these  
 630 features are caused either by zones of narrow strike-slip deformation or antithetic fault-  
 631 ing with regard to the listric marginal faults. This movement appears to have been a long-  
 632 lasting process in the SATZ and is less expressed in the younger sedimentary units.

633 In conclusion, we strongly encourage the application of the proposed diffraction-  
 634 based workflow for high-resolution imaging and depth conversion in future studies. Since  
 635 the presented scheme is likewise applicable to single-channel data, we consider its po-  
 636 tential to be very promising, e.g. in the context of scientific drilling where velocities prior  
 637 to drilling are often only poorly constrained. Moreover, the challenge of correctly identi-  
 638 fying out-of-plane scattering becomes obsolete, if 3D data are considered. Cost-effective  
 639 limited-offset P-cable data are geared towards enabling affordable 3D seismic imaging  
 640 in academic investigations, which makes this emerging data resource an ideal candidate  
 641 for diffraction imaging and inversion across scales and communities (Planke et al., 2009;  
 642 Bauer et al., 2020).

## 643 **Acknowledgments**

644 The authors want to thank Dirk Gajewski for important discussions and assistance and  
 645 Paraskevi Nomikou for providing bathymetric data. We further want to thankfully ac-  
 646 knowledge the support by Charlotte M. Krawczyk and Geo.X, the geoscientific compe-  
 647 tence network in Berlin and Potsdam. Insightful comments and suggestions by A. Malehmir,  
 648 one anonymous reviewer and the associate editor helped to improve this manuscript. This  
 649 work was partially funded by the Federal Ministry for Economic Affairs and Energy of  
 650 Germany (BMW, 03SX427B) and the German Science Foundation (Deutsche Forschungs-  
 651 gemeinschaft, DFG; HU698/25-1) who also funded the acquisition of the seismic data  
 652 in 2006 during cruise POS338. In addition, we are grateful to Schlumberger for provid-  
 653 ing VISTA seismic processing and IHS for providing KINGDOM seismic interpretation  
 654 software. SEG-Y files of the raw pre-stack data and all intermediate steps (the CMP stack  
 655 after SRME, reflection-only data, diffraction-only data, diffraction coherency, inverted  
 656 velocity model, refined velocity model, depth-migrated section, focussed diffractions) are  
 657 available in the Marine Geoscience Data System with data doi: 10.26022/IEDA/327525.  
 658 Codes for diffraction-separation and wavefront tomography are available upon reason-  
 659 able request.

## References

- 660
- 661 Bahorich, M., & Farmer, S. (1995). 3-d seismic discontinuity for faults and strati-  
 662 graphic features: The coherence cube. *The leading edge*, *14*(10), 1053–1058.
- 663 Bakhtiari Rad, P., Schwarz, B., Gajewski, D., & Vanelle, C. (2018). Common-  
 664 reflection-surface-based prestack diffraction separation and imaging. *Geo-*  
 665 *physics*, *83*(1), S47–S55.
- 666 Bauer, A., Schwarz, B., & Gajewski, D. (2016). Enhancement of prestack diffraction  
 667 data and attributes using a travelttime decomposition approach. *Studia Geo-*  
 668 *physica et Geodaetica*, *60*(3), 471–486.
- 669 Bauer, A., Schwarz, B., & Gajewski, D. (2017). Utilizing diffractions in wavefront  
 670 tomography. *Geophysics*, *82*(2), R65–R73.
- 671 Bauer, A., Schwarz, B., & Gajewski, D. (2018). Diffraction wavefront tomography-  
 672 efficient automated velocity inversion for multi-fold and single-channel data. In  
 673 *80th eage conference & exhibition 2018 workshop programme* (pp. cp–556).
- 674 Bauer, A., Schwarz, B., & Gajewski, D. (2020). Velocity inversion and scatterer  
 675 detection with 3D P-Cable data. In *Seg technical program expanded abstracts*  
 676 *2020*.
- 677 Berkovitch, A., Belfer, I., Hassin, Y., & Landa, E. (2009). Diffraction imaging by  
 678 multifocusing. *Geophysics*, *74*(6), WCA75–WCA81.
- 679 Bocchini, G., Brüstle, A., Becker, D., Meier, T., van Keken, P., Ruscic, M., . . .  
 680 Friederich, W. (2018). Tearing, segmentation, and backstepping of subduction  
 681 in the aegean: New insights from seismicity. *Tectonophysics*, *734*, 96–118.
- 682 Bohnhoff, M., Rische, M., Meier, T., Becker, D., Stavrakakis, G., & Harjes, H.  
 683 (2006). Microseismic activity in the hellenic volcanic arc, greece, with emphasis  
 684 on the seismotectonic setting of the santorini–amorgos zone. *Tectonophysics*,  
 685 *423*(1-4), 17–33.
- 686 Chopra, S., & Marfurt, K. J. (2007). *Seismic attributes for prospect identification*  
 687 *and reservoir characterization*. Society of Exploration Geophysicists and Euro-  
 688 pean Association of Geoscientists and Engineers.
- 689 Cossette, É., Audet, P., Schneider, D., & Grasemann, B. (2016). Structure and  
 690 anisotropy of the crust in the cyclades, greece, using receiver functions con-  
 691 strained by in situ rock textural data. *Journal of Geophysical Research: Solid*  
 692 *Earth*, *121*(4), 2661–2678.
- 693 Dafni, R., & Symes, W. (2017). Diffraction imaging by prestack reverse-time migra-  
 694 tion in the dip-angle domain. *Geophysical Prospecting*, *65*, 295–316.
- 695 Decker, L., Janson, X., & Fomel, S. (2015). Carbonate reservoir characterization us-  
 696 ing seismic diffraction imaging. *Interpretation*, *3*(1), SF21–SF30.
- 697 Dell, S., & Gajewski, D. (2011). Common-reflection-surface-based workflow for  
 698 diffraction imaging. *Geophysics*, *76*(5), S187–S195.
- 699 Diekmann, L., Schwarz, B., Bauer, A., & Gajewski, D. (2019). Source localization  
 700 and joint velocity model building using wavefront attributes. *Geophysical Jour-*  
 701 *nal International*, *219*(2), 995–1007.
- 702 Druitt, T., Edwards, L., Mellors, R., Pyle, D., Sparks, R., Lanphere, M., . . . Bar-  
 703 reirio, B. (1999). Santorini volcano. *Geological Society Memoir*, *19*.
- 704 Druitt, T., & Francaviglia, V. (1992). Caldera formation on santorini and the phys-  
 705 iography of the islands in the late bronze age. *Bulletin of Volcanology*, *54*(6),  
 706 484–493.
- 707 Duveneck, E. (2004). Velocity model estimation with data-derived wavefront at-  
 708 tributes. *Geophysics*, *69*(1), 265–274.
- 709 Fomel, S. (2002). Applications of plane-wave destruction filters. *Geophysics*, *67*(6),  
 710 1946–1960.
- 711 Fomel, S., Landa, E., & Taner, M. T. (2007). Poststack velocity analysis by separa-  
 712 tion and imaging of seismic diffractions. *Geophysics*, *72*(6), U89–U94.
- 713 Harding, T. P. (1990). Identification of wrench faults using subsurface structural  
 714 data: criteria and pitfalls. *AAPG bulletin*, *74*(10), 1590–1609.

- 715 Heath, B., Hooft, E., Toomey, D., Papazachos, C., Nomikou, P., Paulatto, M., ...  
 716 Warner, M. (2019). Tectonism and its relation to magmatism around santorini  
 717 volcano from upper crustal p wave velocity. *Journal of Geophysical Research:*  
 718 *Solid Earth*, *124*(10), 10610–10629.
- 719 Hooft, E., Heath, B., Toomey, D., Paulatto, M., Papazachos, C., Nomikou, P., ...  
 720 Warner, M. (2019). Seismic imaging of santorini: Subsurface constraints on  
 721 caldera collapse and present-day magma recharge. *Earth and Planetary Science*  
 722 *Letters*, *514*, 48–61.
- 723 Hooft, E., Nomikou, P., Toomey, D., Lampridou, D., Getz, C., Christopoulou, M.,  
 724 ... others (2017). Backarc tectonism, volcanism, and mass wasting shape  
 725 seafloor morphology in the santorini-christiana-amorgos region of the hellenic  
 726 volcanic arc. *Tectonophysics*, *712*, 396–414.
- 727 Hübscher, C., Hensch, M., Dahm, T., Dehghani, A., Dimitriadis, I., Hort, M., &  
 728 Taymaz, T. (2006). Toward a risk assessment of central aegean volcanoes. *Eos,*  
 729 *Transactions American Geophysical Union*, *87*(39), 401–407.
- 730 Hübscher, C., Ruhnau, M., & Nomikou, P. (2015). Volcano-tectonic evolution of the  
 731 polygenetic kolumbo submarine volcano/santorini (aegean sea). *Journal of Vol-*  
 732 *canology and Geothermal Research*, *291*, 101–111.
- 733 Jäger, R., Mann, J., Höcht, G., & Hubral, P. (2001). Common-reflection-surface  
 734 stack: Image and attributes. *Geophysics*, *66*(1), 97–109.
- 735 Karimpouli, S., Malehmir, A., Hassani, H., Khoshdel, H., & Nabi-Bidhendi, M.  
 736 (2015). Automated diffraction delineation using an apex-shifted radon trans-  
 737 form. *Journal of Geophysics and Engineering*, *12*(2), 199–209.
- 738 Landa, E., & Keydar, S. (1998). Seismic monitoring of diffraction images for detec-  
 739 tion of local heterogeneities. *Geophysics*, *63*(3), 1093–1100.
- 740 Le Pichon, X., & Angelier, J. (1979). The hellenic arc and trench system: a key to  
 741 the neotectonic evolution of the eastern mediterranean area. *Tectonophysics*,  
 742 *60*(1-2), 1–42.
- 743 Le Pichon, X., & Kreemer, C. (2010). The miocene-to-present kinematic evolution of  
 744 the eastern mediterranean and middle east and its implications for dynamics.  
 745 *Annual Review of Earth and Planetary Sciences*, *38*, 323–351.
- 746 Malehmir, A., Schmelzbach, C., Bongajum, E., Bellefleur, G., Juhlin, C., & Tryggva-  
 747 son, A. (2009). 3d constraints on a possible deep > 2.5 km massive sulphide  
 748 mineralization from 2d crooked-line seismic reflection data in the kristineberg  
 749 mining area, northern sweden. *Tectonophysics*, *479*(3-4), 223–240.
- 750 Marfurt, K. J., Kirlin, R. L., Farmer, S. L., & Bahorich, M. S. (1998). 3-d seismic  
 751 attributes using a semblance-based coherency algorithm. *Geophysics*, *63*(4),  
 752 1150–1165.
- 753 Morgan, J., Warner, M., Bell, R., Ashley, J., Barnes, D., Little, R., ... Jones, C.  
 754 (2013). Next-generation seismic experiments: wide-angle, multi-azimuth,  
 755 three-dimensional, full-waveform inversion. *Geophysical Journal International*,  
 756 *195*(3), 1657–1678.
- 757 Moser, T., & Howard, C. (2008). Diffraction imaging in depth. *Geophysical Prospect-*  
 758 *ing*, *56*(5), 627–641.
- 759 Neidell, N. S., & Taner, M. T. (1971). Semblance and other coherency measures for  
 760 multichannel data. *Geophysics*, *36*(3), 482–497.
- 761 Nomikou, P., Druitt, T., Hübscher, C., Mather, T., Paulatto, M., Kalnins, L., ...  
 762 others (2016). Post-eruptive flooding of santorini caldera and implications for  
 763 tsunami generation. *Nature communications*, *7*(1), 1–10.
- 764 Nomikou, P., Hübscher, C., Papanikolaou, D., Farangitakis, G., Ruhnau, M., &  
 765 Lampridou, D. (2018). Expanding extension, subsidence and lateral segmen-  
 766 tation within the santorini-amorgos basins during quaternary: Implications for  
 767 the 1956 amorgos events, central-south aegean sea, greece. *Tectonophysics*,  
 768 *722*, 138–153.
- 769 Nomikou, P., Hübscher, C., Ruhnau, M., & Bejelou, K. (2016). Tectono-

- 770 stratigraphic evolution through successive extensional events of the anydros  
771 basin, hosting kolumbo volcanic field at the aegean sea, greece. *Tectonophysics*,  
772 *671*, 202–217.
- 773 Nomikou, P., Hübscher, C., & Carey, S. (2019). The christiana-santorini-kolumbo  
774 volcanic field. *Elements*, *15*, 171–176.
- 775 Nomikou, P., Papanikolaou, D., Alexandri, M., Sakellariou, D., & Rousakis, G.  
776 (2013). Submarine volcanoes along the aegean volcanic arc. *Tectonophysics*,  
777 *597*, 123–146.
- 778 Nunns, A. G. (1991). Structural restoration of seismic and geologic sections in ex-  
779 tensional regimes (1). *AAPG bulletin*, *75*(2), 278–297.
- 780 Perissoratis, C. (1995). The santorini volcanic complex and its relation to the  
781 stratigraphy and structure of the aegean arc, greece. *Marine Geology*, *128*(1-  
782 2), 37–58.
- 783 Planke, S., Eriksen, F. N., Berndt, C., Mienert, J., & Masson, D. (2009). P-cable  
784 high-resolution seismic. *Oceanography*, *22*(1), 85.
- 785 Sakellariou, D., Sigurdsson, H., Alexandri, M., Carey, S., Rousakis, G., Nomikou,  
786 P., ... Ballas, D. (2010). Active tectonics in the hellenic volcanic arc: the  
787 kolumbo submarine volcanic zone. *Bulletin of the Geological Society of Greece*,  
788 *43*(2), 1056–1063.
- 789 Schwarz, B. (2019a). Coherent wavefield subtraction for diffraction separation. *Geo-*  
790 *physics*, *84*(3), V157–V168.
- 791 Schwarz, B. (2019b). An introduction to seismic diffraction. *Advances in Geophysics*,  
792 *60*.
- 793 Schwarz, B., Bauer, A., & Gajewski, D. (2016). Passive seismic source localiza-  
794 tion via common-reflection-surface attributes. *Studia geophysica et geodaetica*,  
795 *60*(3), 531–546.
- 796 Schwarz, B., & Gajewski, D. (2017). Accessing the diffracted wavefield by coherent  
797 subtraction. *Geophysical Journal International*, *211*(1), 45–49.
- 798 Silvestrov, I., Baina, R., & Landa, E. (2015). Poststack diffraction imaging using  
799 reverse-time migration. *Geophysical Prospecting*, *64*(1), 129–142.
- 800 Tsampouraki-Kraounaki, K., & Sakellariou, D. (2018). Seismic stratigraphy and geo-  
801 dynamic evolution of christiana basin, south aegean arc. *Marine Geology*, *399*,  
802 135–147.
- 803 Verschuur, D. J., Berkhout, A., & Wapenaar, C. (1992). Adaptive surface-related  
804 multiple elimination. *Geophysics*, *57*(9), 1166–1177.
- 805 Virieux, J., & Operto, S. (2009). An overview of full-waveform inversion in explo-  
806 ration geophysics. *Geophysics*, *74*(6), WCC1–WCC26.
- 807 Warner, M., Ratcliffe, A., Nangoo, T., Morgan, J., Umpleby, A., Shah, N., ... others  
808 (2013). Anisotropic 3d full-waveform inversion. *Geophysics*, *78*(2), R59–R80.
- 809 Yin, J., & Nakata, N. (2017). Diffraction imaging with geometric-mean reverse time  
810 migration. In *Seg technical program expanded abstracts 2017* (pp. 974–979). So-  
811 ciety of Exploration Geophysicists.